2D Analytical Calculation of Magnetic Field and electromagnetic Torque for Surface-Inset Permanent Magnet Motors

Thierry Lubin, Smail Mezani, Abderrezak Rezzoug

2D Analytical Calculation of Magnetic Field and Electromagnetic Torque for Surface-Inset Permanent Magnet Motors

Thierry Lubin, Smail Mezani, and Abderrezak Rezzoug

Groupe de Recherche en Electrotechnique et Electronique de Nancy,
University Henri Poincaré, Nancy, FRANCE

The paper deals with a subdomain model for predicting the magnetic field distribution in surface-inset permanent-magnet motors with semi-closed slots under load conditions. Due to the presence of electrical current in the stator slots, a magnetic vector potential formulation is used. The magnetic vector potential distribution in each subdomain (air-gap, stator slots, and rotor slots with inset PMs) is obtained by solving two-dimensional Laplace's and Poisson's equations by the separation of variables method. One of the main contributions of the paper concerns the magnetic vector potential expression in the PMs region. Indeed, PMs are inset into the rotor iron which leads to solve Laplace's equation with nonhomogeneous Neumann boundary conditions. Magnetic field distribution and electromagnetic torque computed with the proposed analytical method are verified with those obtained from finite element analyses.

***Index Terms*— Analytical calculation, Magnetic field distribution, Surface-inset permanent magnet machine, Reluctance torque.**

I. INTRODUCTION

ANALYTICAL models for electrical machines and actuators are based on simplified geometries and often consider infinite permeability for the soft-magnetic material. However, they present less computational time consuming compared to numerical models and provide closed-form solutions giving physical insight for designers. Analytical models are very flexible to compare rapidly different machine topologies and can be useful tools in the first step of design optimization process.

Several models were proposed recently for computing the air-gap magnetic field distribution in PMs motors considering slotting effects. Two analytical methods are mainly developed. The first one is based on Schwarz-Christoffel conformal mapping and provides a 2-D relative permeance function to account for slotting effect [1]-[3]. The actual air-gap flux density is calculated by multiplying the relative permeance function by the radial flux density of a slotless motor. The second one, called the subdomain method, consists in solving directly the Maxwell's equations in the different subdomains i.e. air-gap, stator slots and magnets, by the separation of variables method [4]-[18]. The magnetic field distribution is obtained in each subdomain by using boundary and interface conditions.

In this paper, we present a subdomain model to calculate the magnetic field distribution in surface-inset PMs motors with semi-closed slots under load conditions (Fig. 1). The proposed model can be used for PMs motors with any pole and slot number combinations including fractional-slot machines. Due to the presence of electrical current in the stator slots, a magnetic vector potential formulation is used.

Although some papers were published on the analytical calculation of the magnetic field in surface-inset PMs motors, none was concerned with the analysis of the magnetic field under load conditions. Previous analytical models deal only with no-load conditions. They are all based on a magnetic scalar potential formulation [19]-[22].

This paper extends the model that was presented recently by the authors [23] to a machine with a surface mounted permanent magnet rotor topology. Therefore, we focus essentially on the determination of the magnetic vector potential expression in the rotor PMs region (region *k* of Fig. 1). Indeed, the magnetic vector potential formulation leads to solve Laplace's equation with nonhomogeneous Neumann boundary conditions when the PMs are inset into the rotor iron.

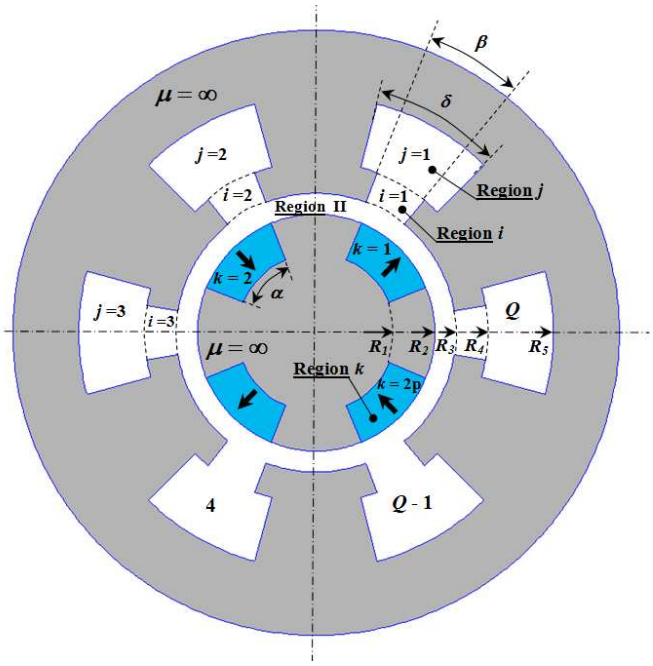

Fig. 1. Surface-inset permanent magnet motor with semi-closed slots (p = 2 and Q = 6).

II. MOTOR GEOMETRY AND ASSUMPTIONS

Fig.1 shows a surface-inset PMs motor with semi-closed

Manuscript received May 19, 2011. Corresponding author: Thierry Lubin. (e-mail: Thierry.Lubin@green.uhp-nancy.fr).
Digital Object Identifier inserted by IEEE

slots. The geometrical parameters are, the inside radius of the permanent magnets R_1, the radius of the rotor R_2, the inner and outer radii of the slot-opening R_3 and R_4 respectively, and R_5 is the radius of the stator slot bottom. The opening angle of the PMs is α, and p is the number of pole pairs (p = 4 in fig. 1). The stator presents Q semi-closed slots (Q = 6 in fig. 1) with current density J_j in each slot. The slot-opening angle (region j in Fig.1) is δ and the slot isthmus angle is β (region i in Fig.1). The analytical model is based on the following assumptions:

- end effects are neglected,
- stator and rotor iron cores are infinitely permeable,
- the PMs are radially magnetized and present a relative recoil permeability μ_r,
- all the boundary surfaces are defined by a constant angle and/or a constant radius.

As shown in Fig.1, the whole domain is divided into four types of subdomains: the $2p$ rotor PMs subdomains (regions k, k=1,2,….,$2p$), the air-gap subdomain (region II), the Q stator slots-opening subdomains (regions i, i=1,2,….,Q) and the Q stator slots subdomains (regions j, j=1,2,….,Q).

The problem is solved in 2D polar coordinates. According to the adopted assumptions, the magnetic vector potential has only one component along the z-direction and only depends on the r and θ coordinates. The notations used in the paper are

$\overrightarrow{A_k} = A_k(r,\theta)\overrightarrow{e_z}$	for the kth rotor PMs subdomain
$\overrightarrow{A_{II}} = A_{II}(r,\theta)\overrightarrow{e_z}$	for the air-gap subdomain
$\overrightarrow{A_i} = A_i(r,\theta)\overrightarrow{e_z}$	for the ith slot-opening subdomain
$\overrightarrow{A_j} = A_j(r,\theta)\overrightarrow{e_z}$	for the jth slot subdomain

where $\overrightarrow{e_z}$ is the unit vector in the z-direction.

Analytical solutions for magnetic vector potential expressions in the air-gap (region II) and in the stator slots subdomains (regions i and j) were presented recently by the authors for a surface-mounted PMs motor [23]. Compared to [23], only the rotor topology is changed and this introduces more difficulties. Hence, in the next section, we focus only on the magnetic vector potential calculation in the PMs rotor subdomain (region k).

III. Analytical Solution of Magnetic Field in the PMs Region

The k-th permanent magnet subdomain is shown in Fig. 2. It is delimited by the radii R_1 and R_2 and by the angles θ_k and $\theta_k+\alpha$. In a frame linked to the stator, the angular position of the k-th PMs region is defined as

$$\theta_k = -\frac{\alpha}{2} + \frac{k\pi}{p} + \Delta \qquad \text{with} \qquad k = 1,2,....2p \qquad (1)$$

where Δ is the mechanical position of the rotor.

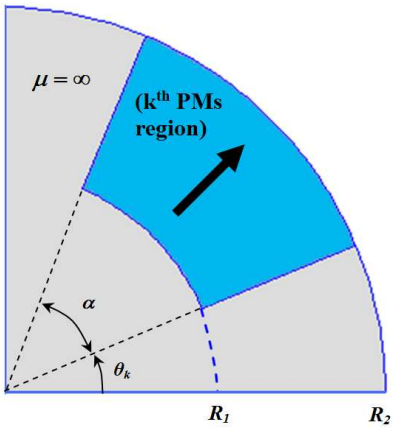

Fig. 2. k-th permanent magnet subdomain.

A. Problem Formulation

The magnetic field in a permanent magnet satisfies the basic equations of magnetostatics

$$\vec{\nabla} \cdot \overrightarrow{B_k} = 0 \qquad (2)$$

$$\vec{\nabla} \times \overrightarrow{H_k} = 0 \qquad (3)$$

where $\overrightarrow{B_k}$ and $\overrightarrow{H_k}$ are respectively the magnetic flux density and the magnetic field vectors in the region k.

The magnetic flux density can be written in terms of the magnetic vector potential $\overrightarrow{A_k}$ as

$$\overrightarrow{B_k} = \vec{\nabla} \times \overrightarrow{A_k} \qquad (4)$$

Modern permanent magnet materials (NdFeB or SmCo) present a linear second quadrant characteristic such as

$$\overrightarrow{B_k} = \mu_0 \mu_r \overrightarrow{H_k} + \mu_0 \overrightarrow{M_k} \qquad (5)$$

where μ_0 is the permeability of air, μ_r is the relative recoil permeability, and $\overrightarrow{M_k}$ is the residual magnetization vector of region k. Equation (3) and (5) are combined to give

$$\vec{\nabla} \times \overrightarrow{B_k} = \mu_0 \vec{\nabla} \times \overrightarrow{M_k} \qquad (6)$$

Using (4) and choosing the Coulomb gauge ($\vec{\nabla} \cdot \overrightarrow{A_k} = 0$), (6) leads to the Poisson equation

$$\nabla^2 \overrightarrow{A_k} = -\mu_0 \vec{\nabla} \times \overrightarrow{M_k} \qquad (7)$$

If we consider that the permanent magnets are radially magnetized with a uniform residual magnetization, the residual magnetization vector in region k can be written as

$$\overrightarrow{M_k} = (-1)^k \frac{B_r}{\mu_0} \overrightarrow{e_r} \qquad \text{with} \qquad k = 1,2,\ldots,2p \qquad (8)$$

where B_r is the remanence of the magnets and $\overrightarrow{e_r}$ the unit vector in the *r*-direction. This reduces the Poisson equation (7) to a Laplace equation

$$\nabla^2 \overrightarrow{A_k} = 0 \tag{9}$$

The magnetic vector potential has an unique component in the z-direction, then (9) becomes

$$\frac{\partial^2 A_k}{\partial r^2} + \frac{1}{r}\frac{\partial A_k}{\partial r} + \frac{1}{r^2}\frac{\partial^2 A_k}{\partial \theta^2} = 0 \tag{10}$$

B. Boundary conditions

The tangential component of the magnetic field along the lateral sides and the bottom of the magnets (iron boundaries) has to be zero because of the infinite permeability for the rotor iron core.

$$\overrightarrow{H_k} \times \vec{n} = \vec{0} \tag{11}$$

where $\vec{n}$ is the unit vector normal to the iron boundaries.

From the constitutive relations (5) and (8), the boundary conditions for the *k*-th PMs subdomain written in terms of magnetic vector potential are given by

$$\left.\frac{\partial A_k}{\partial \theta}\right|_{\theta=\theta_k} = r(-1)^k B_r \tag{12}$$

$$\left.\frac{\partial A_k}{\partial \theta}\right|_{\theta=\theta_k+\alpha} = r(-1)^k B_r \tag{13}$$

$$\left.\frac{\partial A_k}{\partial r}\right|_{r=R_1} = 0 \tag{14}$$

Note that the Neumann boundary conditions (12) and (13) are not homogeneous (not equal to zero) and depend on the *r* coordinate.

The continuity condition between the *k*-th PMs region and the air-gap region leads to

$$A_k(R_2,\theta) = A_{II}(R_2,\theta) \tag{15}$$

where $A_{II}(r,\theta)$ is the magnetic vector potentials in the air-gap which is given by (24) in [23].

C. Solution of Laplace's Equation with Nonhomogeneous Neumann Boundary Conditions

The *k*-th PMs subdomain with its associated boundary conditions is shown in Fig. 3. We have to solve the Laplace equation (10) with nonhomogenous Neumann boundary conditions (12) and (13).

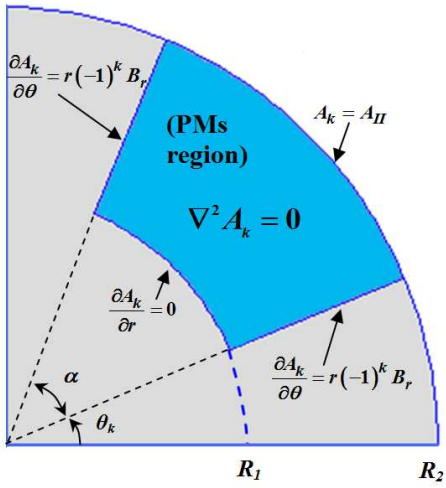

Fig. 3. PMs subdomain (region *k*) with its boundary conditions.

In the separation of variables method, homogeneous boundary conditions are necessary to determine the eigenvalues [25]. Hence, problems with nonhomogeneous boundary conditions need to be transformed to Poisson's equation, with homogeneous boundary conditions.

Using the principle of superposition, the magnetic vector potential $A_k(r,\theta)$ can be expressed as a sum of two functions

$$A_k(r,\theta) = U_k(r,\theta) + V_k(r,\theta) \tag{16}$$

The function $U_k(r,\theta)$ is chosen to satisfy the nonhomogeneous boundary conditions (12) and (13)

$$U_k(r,\theta) = r(-1)^k B_r \theta \tag{17}$$

From (16) and (17), Laplace's equation (10) becomes

$$\frac{\partial^2 V_k}{\partial r^2} + \frac{1}{r}\frac{\partial V_k}{\partial r} + \frac{1}{r^2}\frac{\partial^2 V_k}{\partial \theta^2} = -\frac{1}{r}(-1)^k B_r \theta \tag{18}$$

with homogeneous boundary conditions

$$\left.\frac{\partial V_k}{\partial \theta}\right|_{\theta=\theta_k} = 0 \qquad \left.\frac{\partial V_k}{\partial \theta}\right|_{\theta=\theta_k+\alpha} = 0 \tag{19}$$

It is now possible to use the classical method of separation of variables to solve (18) with homogeneous boundary conditions (19). Eigenvalues and eigenfunctions of the homogeneous problem are given by [16]

$$\lambda_m = \left(\frac{m\pi}{\alpha}\right)^2 \quad \text{with} \quad m = 0,1,2,3,..... \tag{20}$$

$$\Theta_{km}(\theta) = \cos\left(\frac{m\pi}{\alpha}(\theta - \theta_k)\right) \tag{21}$$

The analytic series solution can be written as

$$V_k(r,\theta) = a_0^k + b_0^k \ln r - r\frac{(-1)^k B_r}{2}(2\theta_k + \alpha) + \sum_{m=1}^{\infty}\left(a_m^k r^{\frac{m\pi}{\alpha}} + b_m^k r^{-\frac{m\pi}{\alpha}} - rK_m^k \right)\cos\left(\frac{m\pi}{\alpha}(\theta-\theta_k)\right) \quad (22)$$

where a_0^k, b_0^k, a_m^k and b_m^k are arbitrary constants and K_m^k is defined as

$$K_m^k = \frac{2\alpha(-1)^k B_r\left(1-(-1)^m\right)}{(m\pi)^2\left(\left(\frac{m\pi}{\alpha}\right)^2 - 1\right)} \quad (23)$$

Substituting (17) and (22) into (16) and taking into account the boundary conditions (14) and the interface condition (15), the general solution of the magnetic vector potential in region *k* can be written as

$$A_k(r,\theta) = c_0^k + r(-1)^k B_r\left(\theta-\theta_k-\frac{\alpha}{2}\right) + \sum_{m=1}^{\infty} c_m^k \frac{P_{m\pi/\alpha}(r,R_1)}{P_{m\pi/\alpha}(R_2,R_1)}\cos\left(\frac{m\pi}{\alpha}(\theta-\theta_k)\right) - \sum_{m=1}^{\infty} K_m^k\left(r + \frac{m\pi R_1}{\alpha}\left(\frac{r}{R_1}\right)^{-\frac{m\pi}{\alpha}}\right)\cos\left(\frac{m\pi}{\alpha}(\theta-\theta_k)\right) \quad (24)$$

where c_0^k and c_m^k are new integration constants and

$$P_{m\pi/\alpha}(r,R_1) = \left(\frac{r}{R_1}\right)^{\frac{m\pi}{\alpha}} + \left(\frac{r}{R_1}\right)^{-\frac{m\pi}{\alpha}} \quad (25)$$

The integration constants c_0^k and c_m^k are determined using a Fourier series expansion of the air-gap magnetic vector potential $A_{II}(R_2,\theta)$ (equation (24) in [23]) over the interval $[\theta_k, \theta_k+\alpha]$.

$$c_0^k = \frac{1}{\alpha}\int_{\theta_k}^{\theta_k+\alpha} A_{II}(R_2,\theta)\,d\theta \quad (26)$$

$$c_m^k = K_m^k\left(\frac{R_1 m\pi}{\alpha}\left(\frac{R_1}{R_2}\right)^{\frac{m\pi}{\alpha}} + R_2\left(\frac{m\pi}{\alpha}\right)^2\right) + \frac{2}{\alpha}\int_{\theta_k}^{\theta_k+\alpha} A_{II}(R_2,\theta)\cos\left(\frac{m\pi}{\alpha}(\theta-\theta_k)\right)d\theta \quad (27)$$

Expressions of the coefficients c_0^k, and c_m^k are given in the appendix.

The radial and tangential flux densities B_k^r and B_k^θ in the PMs regions are deduced from the magnetic vector potential expression (24) by

$$\overrightarrow{B_k} = B_k^r(r,\theta)\overrightarrow{e_r} + B_k^\theta(r,\theta)\overrightarrow{e_\theta} \quad (28)$$

with

$$B_k^r = \frac{1}{r}\frac{\partial A_k}{\partial\theta} \qquad B_k^\theta = -\frac{\partial A_k}{\partial r} \quad (29)$$

Their expressions are

$$B_k^r(r,\theta) = (-1)^k B_r - \sum_{m=1}^{\infty} c_m^k \frac{m\pi}{\alpha r}\frac{P_{m\pi/\alpha}(r,R_1)}{P_{m\pi/\alpha}(R_2,R_1)}\sin\left(\frac{m\pi}{\alpha}(\theta-\theta_k)\right) + \sum_{m=1}^{\infty} K_m^k \frac{m\pi}{\alpha r}\left(r + \frac{m\pi R_1}{\alpha}\left(\frac{r}{R_1}\right)^{-\frac{m\pi}{\alpha}}\right)\sin\left(\frac{m\pi}{\alpha}(\theta-\theta_k)\right) \quad (30)$$

$$B_k^\theta(r,\theta) = -(-1)^k B_r\left(\theta-\theta_k-\frac{\alpha}{2}\right) - \sum_{m=1}^{\infty} c_m^k \frac{m\pi}{\alpha r}\frac{E_{m\pi/\alpha}(r,R_1)}{P_{m\pi/\alpha}(R_2,R_1)}\cos\left(\frac{m\pi}{\alpha}(\theta-\theta_k)\right) + \sum_{m=1}^{\infty} K_m^k\left(1-\left(\frac{m\pi}{\alpha}\right)^2\frac{R_1}{r}\left(\frac{r}{R_1}\right)^{-\frac{m\pi}{\alpha}}\right)\cos\left(\frac{m\pi}{\alpha}(\theta-\theta_k)\right) \quad (31)$$

where

$$E_{m\pi/\alpha}(r,R_1) = \left(\frac{r}{R_1}\right)^{\frac{m\pi}{\alpha}} - \left(\frac{r}{R_1}\right)^{-\frac{m\pi}{\alpha}} \quad (32)$$

D. Integration Constants for the Air-gap Region

Compared to the problem linked to the machine with surface-mounted permanent-magnets [23], if the boundary condition for $r = R_3$ are the same and lead to the same coefficient expressions b_n^{II} and d_n^{II}, the ones on $r = R_2$ must be totally reconsidered in the case of the present machine. The constants a_n^{II} and c_n^{II} have to be re-written as

$$a_n^{II} = \frac{2}{2\pi}\sum_{k=1}^{2p}\int_{\theta_k}^{\theta_k+\alpha}\frac{1}{\mu_r}\frac{\partial A_k}{\partial r}\bigg|_{r=R_2}\cos(n\theta)\,d\theta \quad (33)$$

$$c_n^{II} = \frac{2}{2\pi}\sum_{k=1}^{2p}\int_{\theta_k}^{\theta_k+\alpha}\frac{1}{\mu_r}\frac{\partial A_k}{\partial r}\bigg|_{r=R_2}\sin(n\theta)\,d\theta \quad (34)$$

where μ_r is the relative permeability of the magnets. The coefficients a_n^{II} and c_n^{II} are developed in the appendix.

IV. Analytical Results and Comparison with Finite Element Calculation

In order to validate the proposed model, the analytical results are compared with those obtained from 2D FEM simulations [24] when the same assumptions are used. The mesh in the different regions is refined until convergent results are obtained. The flux density in the air-gap, in the PMs, and in the slot-opening and slots regions are computed with a finite number of harmonic terms N_I and $N_{i,j,k}$ as it is indicated in Table I.

As an example of surface-inset PMs machine, we investigate here the performances of a three-phase fractional-slot PMs motor. This machine presents 4-pole/15-slot corresponding to a number of slot per pole and per phase equal to q = 1.25. The geometrical parameters used in the simulation studies are given in Table I.

This fractional slot machine has a double-layer winding with a coil pitch equals to 3 slots. Fig. 4 shows the windings distribution in the stator slots.

The corresponding connecting matrix that represents the stator windings distribution in the slots is

$$[C]=\begin{bmatrix} 2 & 1 & 0 & -1 & -2 & 0 & 0 & 1 & 1 & 0 & 0 & -1 & -1 & 0 & 0 \\ 0 & -1 & -1 & 0 & 0 & 2 & 1 & 0 & -1 & -2 & 0 & 0 & 1 & 1 & 0 \\ 0 & 0 & 1 & 1 & 0 & 0 & -1 & -1 & 0 & 0 & 2 & 1 & 0 & -1 & -2 \end{bmatrix} \quad (35)$$

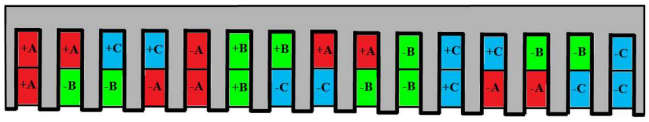

Fig. 4. Double-layer windings distribution for a three phases machine with 15 slots and p = 2 (q = 1.25).

TABLE I
Parameters of the Surface-Inset PMs Machine

Symbol	Quantity	value
R_1	Inner radius of the PMs	3.2 cm
R_2	Radius of the rotor surface	4 cm
R_3	Stator bore radius	4.1 cm
R_4	Outer radius of the slot-opening	4.3 cm
R_5	Outer radius of the slot	5.3 cm
L	Axial length	20 cm
δ	Slot-opening angle	*12°*
β	Slot isthmus angle	*6°*
α	PMs opening angle	45°
B_r	Remanence of the permanent magnets	1.2 T
μ_r	Relative recoil permeability	1.05
p	Pole-pairs number	2
Q	Number of stator slots	15
J_{rms}	RMS current density	4 A/mm²
N_I	Number of harmonics used for magnetic field calculation in the air-gap domain	100
$N_{i,j,k}$	Number of harmonics used for magnetic field calculation in the slot, slot-opening and PMS domains	50

1) Results for No-Load Condition (B_r = 1.2T and J_{rms}=0 A/mm²)

Figure 5 shows the magnetic flux lines in the machine under no-load condition. The radial and tangential components of the flux density in the middle of the air-gap (at $r = 4.05cm$) are shown in Fig. 6. Excellent agreement is obtained between analytical and FE results. One can see clearly the distortion of the radial component of the flux density at the location of the slot-opening placed in front of the magnets. For no-load condition, we can observe that the air-gap flux density is null in front of the rotor saliency.

Using (30) and (31), the radial and tangential components of the flux density in the 1st PMs region (k=1; at $r = 3.6cm$ and 22.5°< θ <67.5°) are calculated and plotted in Fig. 7. In accordance with the boundary conditions (12) and (13) used in the analytical model, one can observe that the radial component of the magnetic field at the sides of the magnet is equal to the remanence B_r. Due to the demagnetization effect (air-gap and slots), one can observe on Fig. 7a that the radial component of the flux density is somewhat lower than the remanence of the magnet. Fig. 7b shows that it is difficult to predict accurately the tangential component of the flux density with FEM [24] when PMs are inset into the rotor iron, despite using a very fine mesh size.

The analytical determination of the back-EMF waveform as a function of the rotor position for n_{turn}=1 is presented in Fig. 8. The computation is done for a rotating speed Ω = 1500 rpm. The maximum value of the back-EMF is around 10V. The analytical and numerical predictions are close to less than 1%.

The cogging torque is given in Fig.9. The torque is evaluated at consecutive rotor positions using Maxwell stress tensor method. The angular period of the cogging torque corresponds to the Least Common Multiple of 2p and Q giving 360°/*LCM*(Q,2p)=6°. It can be seen that the proposed analytical model can predict the cogging torque with an excellent precision.

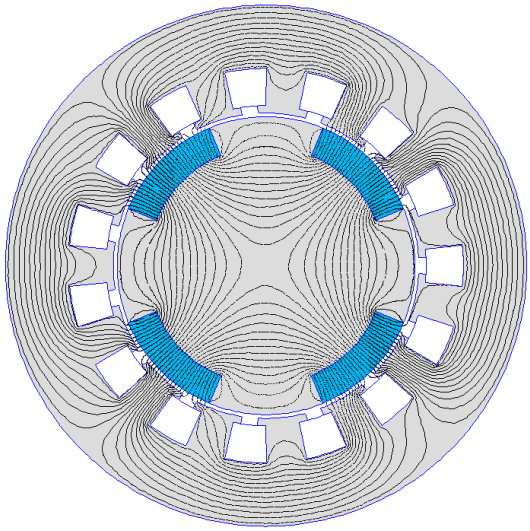

Fig. 5. Magnetic flux distribution for no-load condition obtained with FEM.

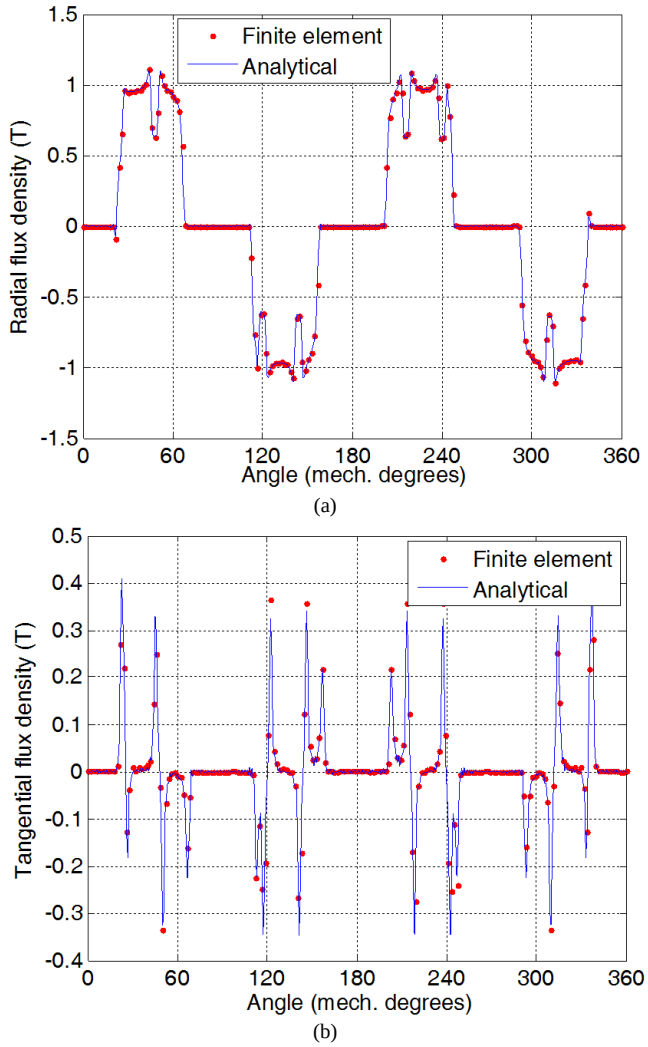

Fig. 6. Radial (a) and tangential (b) components of the flux density for no load condition in the middle of the air-gap.

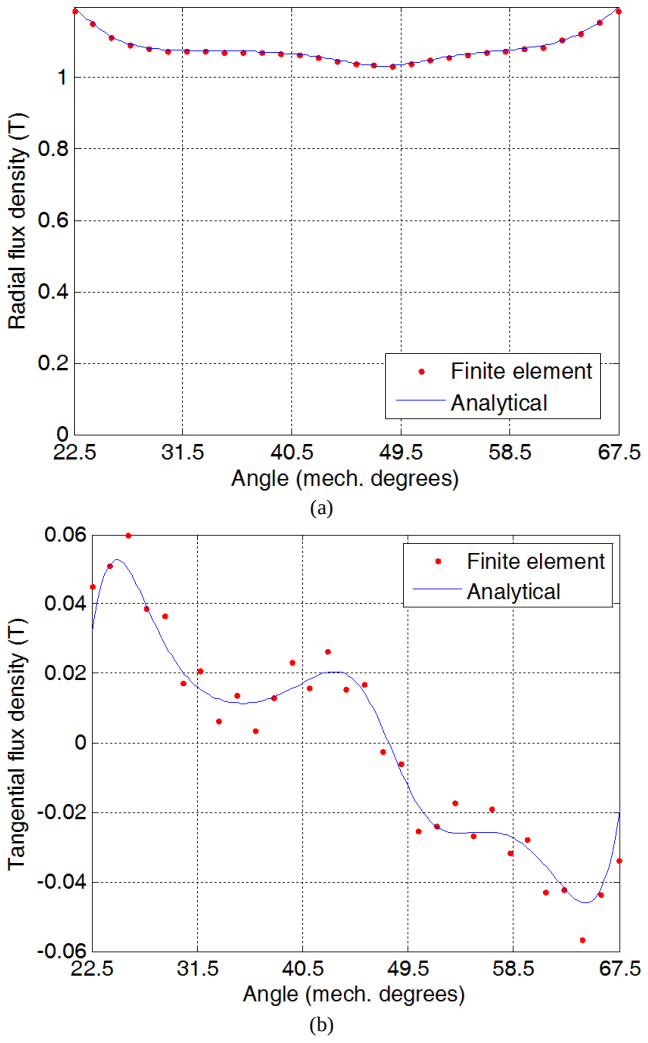

Fig. 7. Radial (a) and tangential (b) components of the flux density for no load condition in the 1st PMs region (k=1) at $r=(R_1+R_2)/2$.

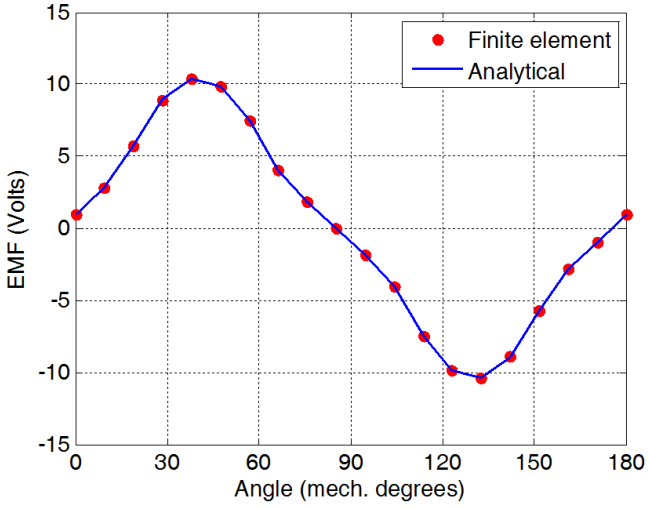

Fig. 8. Per turn phase back-EMF waveform.

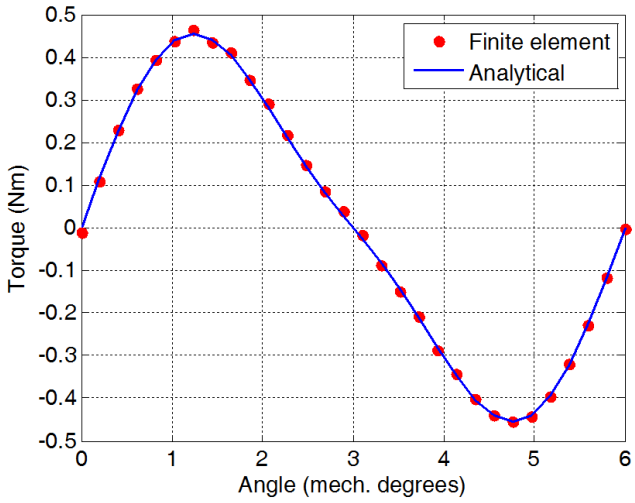

Fig. 9. Cogging torque waveform.

2) Armature Reaction Field (B_r = 0T and J_{rms}=4A/mm²)

Figure 10 shows the flux distribution in the machine caused by the armature reaction acting alone. The magnets are removed and replaced by air. The three-phase stator windings are fed with electrical current such as $I_a = I$ and $I_b = I_c = -I/2$ corresponding to AC operation. Fig. 11 and Fig. 12 compare the FE and analytically predicted flux density waveforms in the air-gap and PM regions. Fig. 12a shows that the radial component of the flux density is now equal to zero at the iron boundaries.

Due to its rotor saliency (the reactance X_d is smaller than X_q), this motor develops a reluctance torque. Fig. 13 shows the comparison between analytical and FE predictions for the static reluctance torque. As expected, the reluctance torque reaches its maximum value for an angle of about 22.5°. Fig. 14 shows the electromagnetic torque waveform versus rotor position for a control angle giving the maximum torque. At each rotor position, the current values in the different slots are updated to have a sinusoidal current waveform. It can be seen that the studied machine produces an average reluctance torque of about 5.5 Nm. The proposed analytical model can predict the reluctance torque with a very good precision.

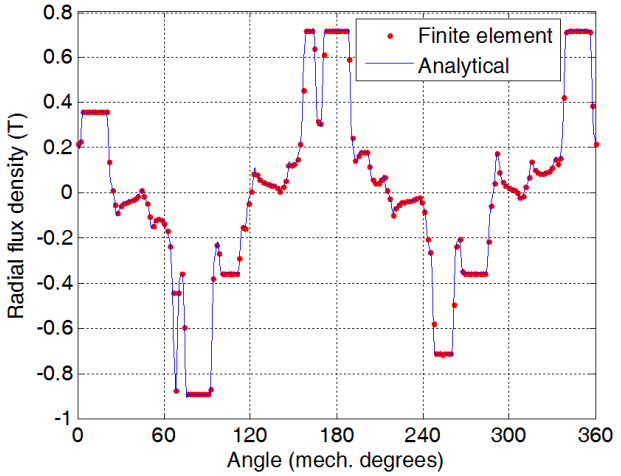

(a)

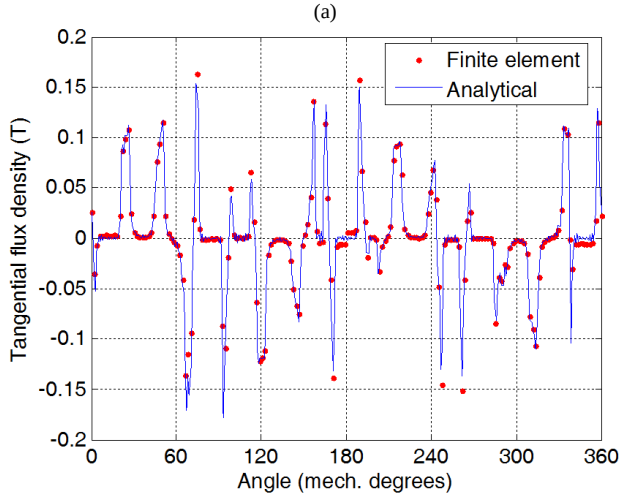

(b)

Fig. 11. Flux density distribution for radial (a) and tangential (b) components of armature reaction field in the middle of the air-gap for J_{rms}=4A/mm², $I_a = I$ and $I_b = I_c = -I/2$.

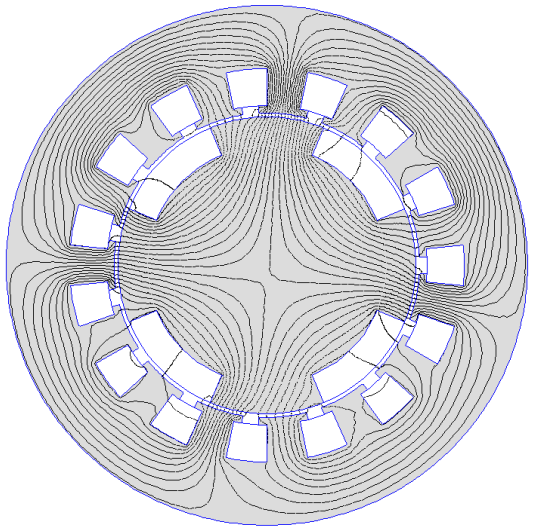

Fig. 10. Armature reaction magnetic flux distribution obtained with FEM for J_{rms}=4A/mm² (the magnets are removed).

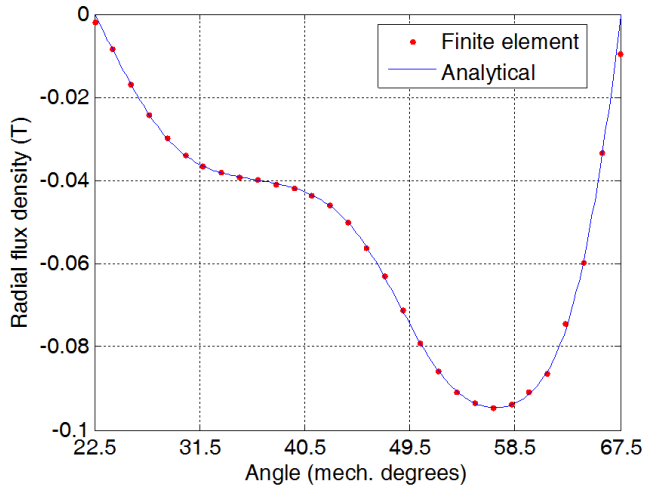

(a)

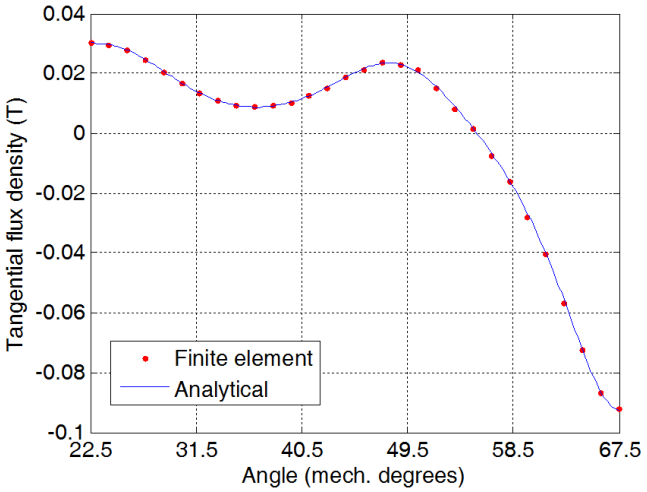

(b)

Fig. 12. Flux density distribution for radial (a) and tangential (b) components of armature reaction in the 1st PMs region (k=1) at $r=(R_1+R_2)/2$.

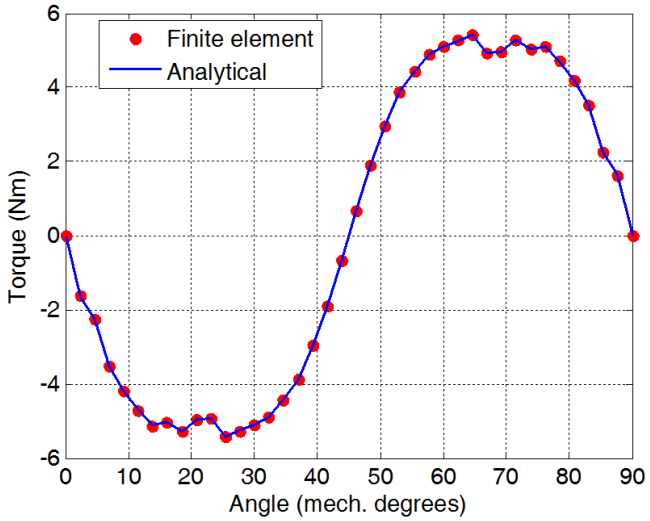

Fig. 13. Static torque versus rotor position due to slots currents alone (reluctance torque) for J_{rms}=4 *A/mm²*.

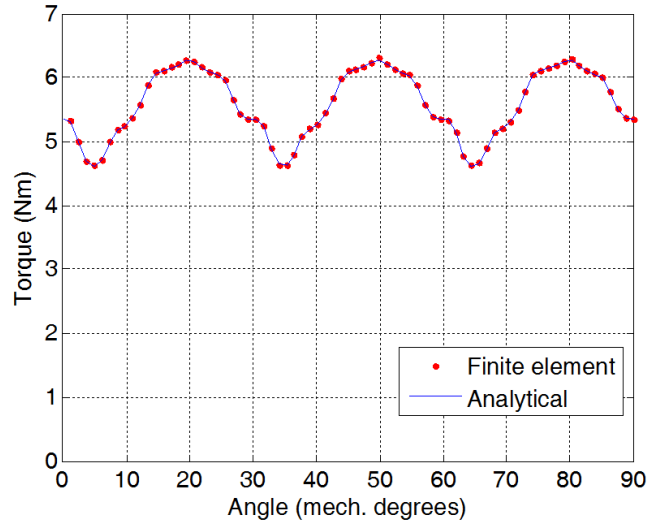

Fig. 14. Electromagnetic torque versus rotor position due to slots currents alone (reluctance torque) for J_{rms}=4*A/mm²*.

3) Results for Load Condition (B_r =1.2T,J_{rms}=4A/mm²)

Figure 15 shows the flux distribution due to both PMs and armature current (load condition). The three-phase stator windings are fed so that $I_a = I$ and $I_b = I_c = -I/2$ corresponding to AC operation (J_{rms} = 4*A/mm²*). The radial and tangential components of the flux density in the air-gap and magnet regions are respectively shown in Fig. 16 and Fig. 17. The influence of the armature reaction on both radial and tangential components of the flux density waveforms is noticeable in comparison with the no-load results of Fig. 6 and Fig. 7.

The static torque versus mechanical rotor position is presented in Fig. 18. Maximum torque occurs at an angle of about 60°. It is well-known that for a surface-inset PMs motor, the maximum torque occurs at an angle greater than 45°. Surface-inset PMs motors produce not only permanent magnets torque component (for which the maximum torque value occurs at an angle of 45°) but also reluctance torque component as shown in Fig. 13.

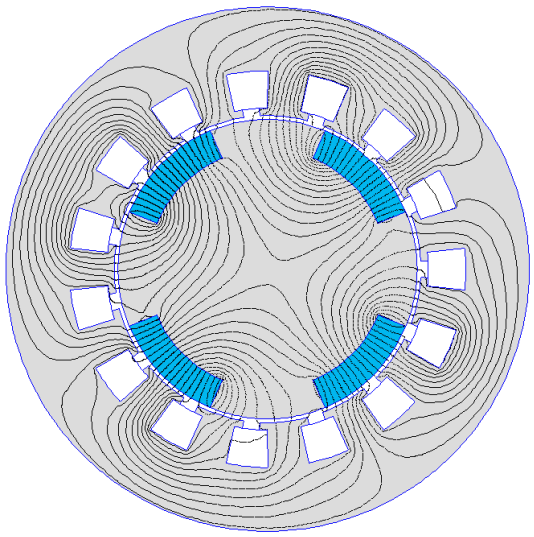

Fig. 15. Magnetic flux distribution for load condition.

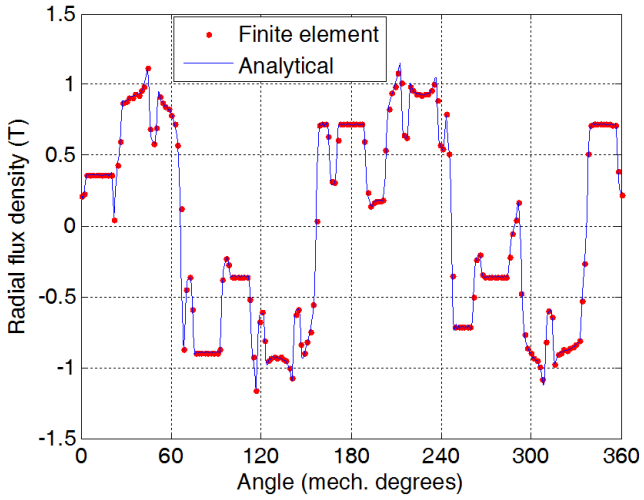

(a)

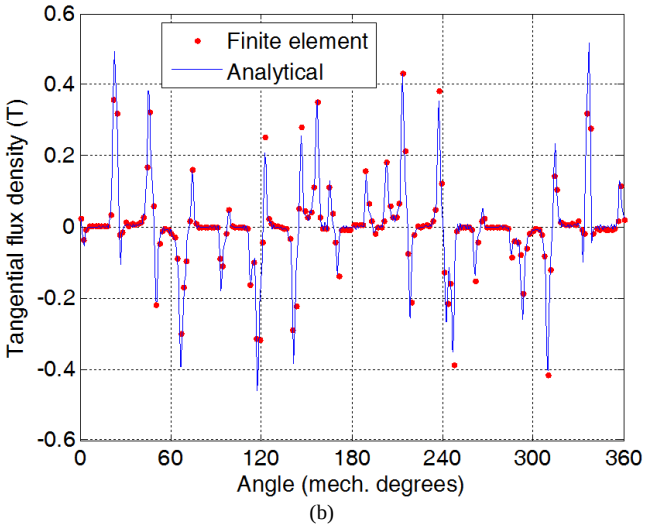

(b)

Fig. 16. Radial (a) and tangential (b) flux density distribution in the middle of the air-gap for load condition.

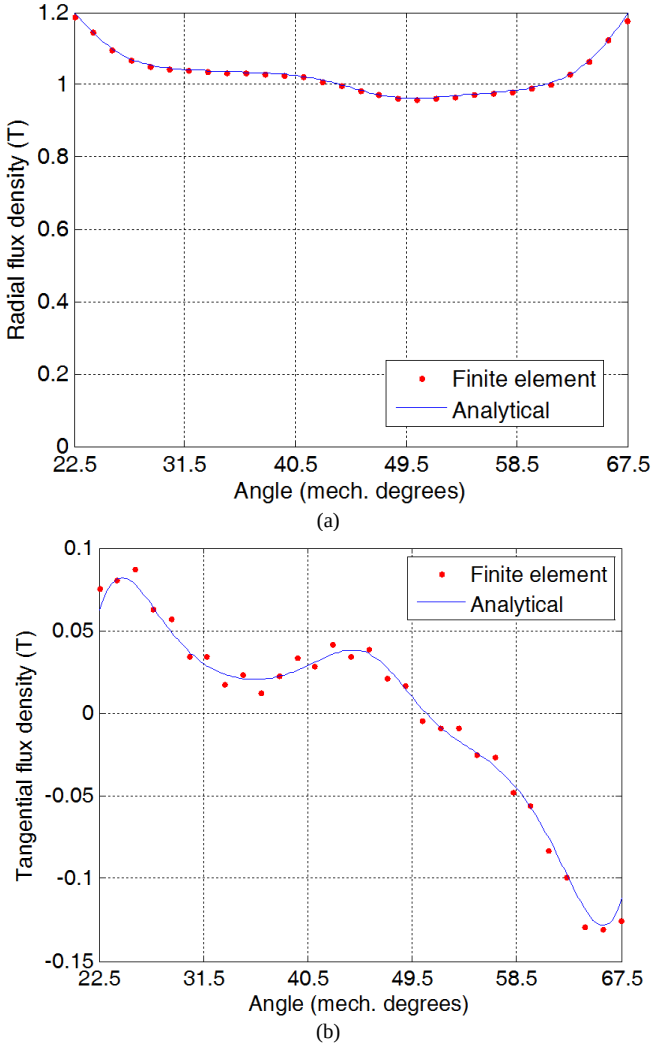

Fig. 17. Flux density distribution for radial (a) and tangential (b) component in the 1st PMs region (k=1) at $r=(R_1+R_2)/2$ for load condition.

Figure 19 shows the electromagnetic torque waveform versus rotor position. At each rotor position, the current values in the different slots are updated to have a sinusoidal current waveform. It can be seen that the studied machine produces an average torque of about 26 Nm. The torque ripples are due to cogging torque (Fig. 9) and reluctance torque (Fig. 14). If we compare Fig. 14 and Fig. 19, one can observe that the mean value of the reluctance torque is about 20% of the total torque. Once again, the analytical and the FEM results are in good accordance.

In order to have a good precision in the analytical torque evaluation, the number of harmonic terms in each region should be chosen carefully. In our case, a number of harmonic terms equal to N_I = 30 for the air-gap region and $N_{i,j,k}$=10 for the slots, slot-opening and PMs regions gives a good precision. For a given rotor position, the computation time is about 70 ms with the analytical model whereas the linear FEM takes about 3 s for a mesh of 33500 elements. The analytical computations being much faster, the presented model can advantageously be used in a preliminary design of surface-inset PMs motors.

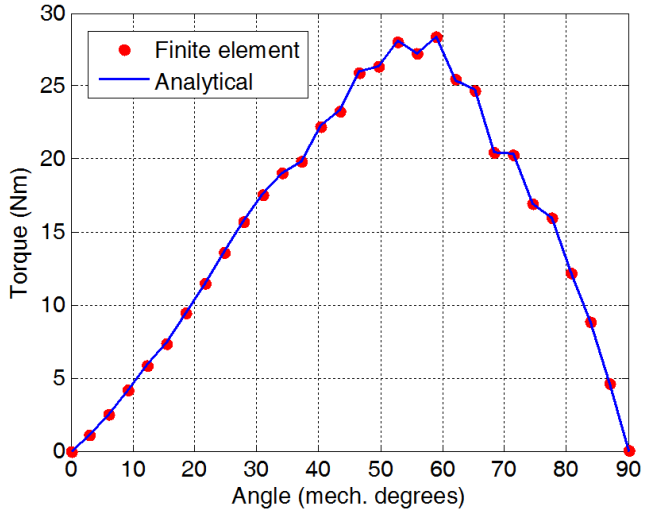

Fig. 18. Static torque versus rotor position for J_{rms}=4A/mm².

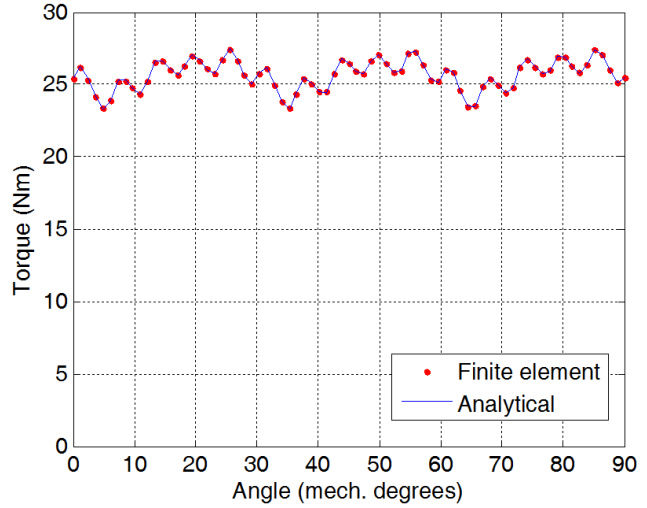

Fig. 19. Electromagnetic torque versus rotor position for J_{rms}=4A/mm².

4) Model Limitations due to Magnetic Saturation

In order to study the model limitations due to magnetic saturation of the iron parts, we have compared the maximum torque value obtained with the analytical model (which considers infinite permeability of the iron parts) with the one obtained by nonlinear finite elements analysis [24]. The $B(H)$ characteristic used in FE simulations is shown in Fig. 20 (knee point of around 1.6T). This curve corresponds to M-27 steel given in the FEMM software [24].

Figure 21 shows the maximum torque as a function of the current density obtained with the analytical model and with FE simulations (the geometrical parameters are those given in Table I). In order to show the effect of the magnetic saturation, we have considered different values for the current density in the slots (J_{rms} = 2 A/mm^2 to J_{rms} = 12 A/mm^2). As expected, the maximum torque obtained with nonlinear FE analysis is below the analytical prediction especially for large value of the current density.

Nevertheless, as it can be observed in Fig. 21, the infinite permeability assumption of the stator/rotor back iron has a low

impact on the accuracy of the torque determination for the studied machine working in normal conditions (error less than 4% for for $J_{rms} \leq 6$ A/mm^2). This is due to the fact that PM machines usually have a large air-gap (1mm for the studied machine) and that the relative permeability of magnets is very close to unity (μ_r = 1.05). Therefore the reluctance of the effective air-gap is considerably higher compared to that of the stator and rotor back-iron. So, the stator teeth are not highly saturated, except for large values of the current density.

V. Conclusion

In this paper, an analytical approach to calculate the magnetic field distribution in surface-inset PM motors, including both stator slotting effects (semi-closed slots) and rotor saliency, was developed. The proposed model is sufficiently general to be used for any poles and slots combination including fractional slot winding machines. Flux density distribution, back-EMF and electromagnetic torque computations for no-load and load conditions are favorably compared to those issued from finite element simulations.

As the analytical model is less computational time consuming than FEM, it can advantageously be used in the initial design and optimization of surface-inset PMs motors.

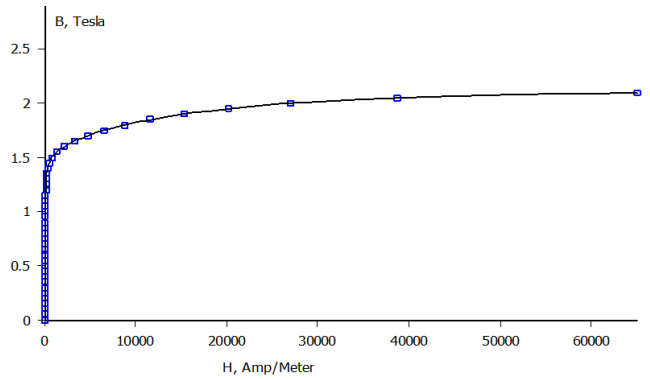

Fig. 20. *B*(*H*) characteristic of the stator/rotor back iron used in nonlinear FE simulations.

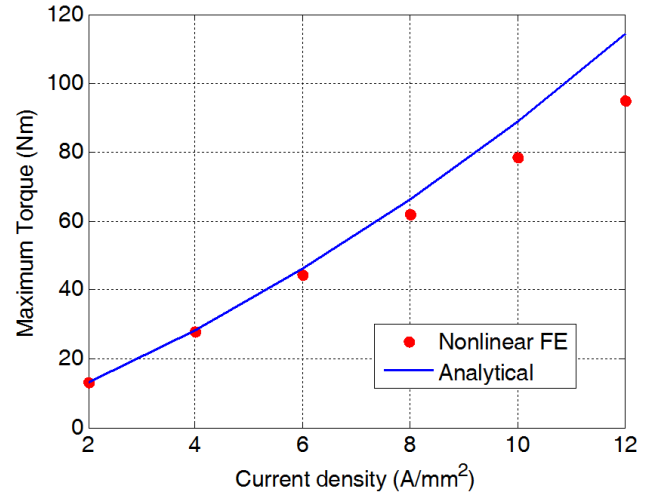

Fig. 21. Maximum torque versus current density computed with analytical model and nonlinear FE simulations.

Appendix

For the determination of the integration coefficients in the different regions, we have to calculate integrals of the form

$$f(k,n,i) = \int_{\theta_i}^{\theta_i+\beta} \cos(n\theta)\cdot\cos\left(\frac{k\pi}{\beta}(\theta-\theta_i)\right)\cdot d\theta \qquad \text{(A.1)}$$

$$g(k,n,i) = \int_{\theta_i}^{\theta_i+\beta} \sin(n\theta)\cdot\cos\left(\frac{k\pi}{\beta}(\theta-\theta_i)\right)\cdot d\theta \qquad \text{(A.2)}$$

$$r(n,i) = \int_{\theta_i}^{\theta_i+\beta} \cos(n\theta)\cdot d\theta \qquad \text{(A.3)}$$

$$s(n,i) = \int_{\theta_i}^{\theta_i+\beta} \sin(n\theta)\cdot d\theta \qquad \text{(A.4)}$$

$$F(m,k) = \int_{\theta_i}^{\theta_i+\beta} \cos\left(\frac{m\pi}{\delta}(\theta-\theta_i-\frac{1}{2}(\beta-\delta))\right)\cos\left(\frac{k\pi}{\beta}(\theta-\theta_i)\right)d\theta \qquad \text{(A.5)}$$

The calculations of the previous integrals lead to the following results:

- for $k\pi \neq n\beta$

$$f(k,n,i) = \frac{-n\beta^2\left((-1)^k \sin n(\beta+\theta_i) - \sin(n\theta_i)\right)}{k^2\pi^2 - n^2\beta^2} \qquad \text{(A.6)}$$

$$g(k,n,i) = \frac{n\beta^2\left((-1)^k \cos n(\beta+\theta_i) - \cos(n\theta_i)\right)}{k^2\pi^2 - n^2\beta^2} \qquad \text{(A.7)}$$

- for $k\pi = n\beta$

$$f(k,n,i) = \frac{\beta}{2}\left(\cos(n\theta_i) + \frac{1}{2k\pi}\left(\sin n(\theta_i+2\beta) - \sin(n\theta_i)\right)\right) \qquad \text{(A.8)}$$

$$g(k,n,i) = \frac{\beta}{2}\left(\sin(n\theta_i) - \frac{1}{2k\pi}\left(\cos n(\theta_i+2\beta) - \cos(n\theta_i)\right)\right) \qquad \text{(A.9)}$$

The development of (A.3) and (A.4) gives

$$r(n,i) = \frac{1}{n}\left(\sin(n\theta_i+n\beta) - \sin(n\theta_i)\right) \qquad \text{(A.10)}$$

$$s(n,i) = \frac{1}{n}\left(-\cos(n\theta_i+n\beta) + \cos(n\theta_i)\right) \qquad \text{(A.11)}$$

The development of (A.5) gives

- for $\frac{m\pi}{\delta} \neq \frac{k\pi}{\beta}$

$$F(m,k) = \frac{\frac{m\pi}{\delta}}{\left(\frac{m\pi}{\delta}\right)^2 - \left(\frac{k\pi}{\beta}\right)^2} \times \left\{(-1)^k \sin\left(\frac{m\pi}{2\delta}(\beta+\delta)\right) + \sin\left(\frac{m\pi}{2\delta}(\beta-\delta)\right)\right\} \qquad \text{(A.12)}$$

- for $\frac{m\pi}{\delta}=\frac{k\pi}{\beta}$

$$F(m,k)=\frac{\beta}{2}\cos\left(\frac{k\pi}{2\beta}(\beta-\delta)\right) \tag{A.13}$$

• Expressions of the coefficients a_n^{II} , b_n^{II} , c_n^{II} and d_n^{II} for the air-gap subdomain

The development of (33) and (34) gives

$$\begin{aligned}a_n^{II}=&\sum_{k=1}^{2p}\frac{(-1)^k B_r}{\mu_r\pi}\left(\frac{\alpha}{2n}\left(\sin(n(\theta_k+\alpha))+\sin(n\theta_k)\right)-\frac{1}{n}s(n,k)\right)\\&-\sum_{k=1}^{2p}\sum_{m=1}^{\infty}c_m^k\frac{1}{\mu_r}\frac{m}{\alpha R_2}\frac{E_{m\pi/\alpha}(R_1,R_2)}{P_{m\pi/\alpha}(R_1,R_2)}f(m,n,k)\\&-\sum_{k=1}^{2p}\sum_{m=1}^{\infty}\frac{K_m^k}{\mu_r\pi}\left(1-\left(\frac{m\pi}{\alpha}\right)^2\left(\frac{R_1}{R_2}\right)^{\left(\frac{m\pi}{\alpha}+1\right)}\right)f(m,n,k)\end{aligned} \tag{A.14}$$

$$\begin{aligned}c_n^{II}=&\sum_{k=1}^{2p}\frac{(-1)^k B_r}{\mu_r\pi}\left(-\frac{\alpha}{2n}\left(\cos(n(\theta_k+\alpha))+\cos(n\theta_k)\right)+\frac{1}{n}r(n,k)\right)\\&-\sum_{k=1}^{2p}\sum_{m=1}^{\infty}c_m^k\frac{1}{\mu_r}\frac{m}{\alpha R_2}\frac{E_{m\pi/\alpha}(R_1,R_2)}{P_{m\pi/\alpha}(R_1,R_2)}g(m,n,k)\\&-\sum_{k=1}^{2p}\sum_{m=1}^{\infty}\frac{K_m^k}{\mu_r\pi}\left(1-\left(\frac{m\pi}{\alpha}\right)^2\left(\frac{R_1}{R_2}\right)^{\left(\frac{m\pi}{\alpha}+1\right)}\right)g(m,n,k)\end{aligned} \tag{A.15}$$

where K_m^k is given by (23).

The coefficient b_n^{II} and c_n^{II} defined in [23] are given by

$$\begin{aligned}b_n^{II}=&\sum_{i=1}^{Q}\frac{b_0^i}{\pi R_3}r(n,i)\\&+\sum_{i=1}^{Q}\sum_{k=1}^{\infty}a_k^i\frac{k}{\beta R_3}\frac{P_{k\pi/\beta}(R_3,R_4)}{E_{k\pi/\beta}(R_3,R_4)}f(k,n,i)\\&-\sum_{i=1}^{Q}\sum_{k=1}^{\infty}b_k^i\frac{k}{\beta R_3}\frac{2}{E_{k\pi/\beta}(R_3,R_4)}f(k,n,i)\end{aligned} \tag{A.16}$$

$$\begin{aligned}d_n^{II}=&\sum_{i=1}^{Q}\frac{b_0^i}{\pi R_3}s(n,i)\\&+\sum_{i=1}^{Q}\sum_{k=1}^{\infty}a_k^i\frac{k}{\beta R_3}\frac{P_{k\pi/\beta}(R_3,R_4)}{E_{k\pi/\beta}(R_3,R_4)}g(k,n,i)\\&-\sum_{i=1}^{Q}\sum_{k=1}^{\infty}b_k^i\frac{k}{\beta R_3}\frac{2}{E_{k\pi/\beta}(R_3,R_4)}g(k,n,i)\end{aligned} \tag{A.17}$$

where Q is the number of stator slots.

• Expressions of coefficients c_0^k and c_m^k for the PMs subdomain :

The calculation of (26) and (27) yields to the following linear relations between the integration constants in the PMs and air-gap subdmains

$$\begin{aligned}c_0^k=&\sum_{n=1}^{\infty}\left(a_n^{II}\frac{R_2}{n\alpha}\frac{P_n(R_2,R_3)}{E_n(R_2,R_3)}+b_n^{II}\frac{R_3}{n\alpha}\frac{2}{E_n(R_3,R_2)}\right)r(n,k)\\&+\sum_{n=1}^{\infty}\left(c_n^{II}\frac{R_2}{n\alpha}\frac{P_n(R_2,R_3)}{E_n(R_2,R_3)}+d_n^{II}\frac{R_3}{n\alpha}\frac{2}{E_n(R_3,R_2)}\right)s(n,k)\end{aligned} \tag{A.18}$$

$$\begin{aligned}c_m^k=&\sum_{n=1}^{\infty}\left(a_n^{II}\frac{2R_2}{n\alpha}\frac{P_n(R_2,R_3)}{E_n(R_2,R_3)}+b_n^{II}\frac{2R_3}{n\alpha}\frac{2}{E_n(R_3,R_2)}\right)f(m,n,k)\\&+\sum_{n=1}^{\infty}\left(c_n^{II}\frac{2R_2}{n\alpha}\frac{P_n(R_2,R_3)}{E_n(R_2,R_3)}+d_n^{II}\frac{2R_3}{n\alpha}\frac{2}{E_n(R_3,R_2)}\right)g(m,n,k)\\&+K_m^k\left(\frac{R_1 m\pi}{\alpha}\left(\frac{R_1}{R_2}\right)^{\frac{m\pi}{\alpha}}+R_2\left(\frac{m\pi}{\alpha}\right)^2\right)\end{aligned} \tag{A.19}$$

• Expression of coefficients a_0^i, b_0^i, a_k^i and b_k^i for the *i*th slot-opening subdomain

$$\begin{aligned}a_k^i=&\sum_{n=1}^{\infty}(a_n^{II}\frac{2R_2}{n\beta}\frac{2}{E_n(R_2,R_3)}+b_n^{II}\frac{2R_3}{n\beta}\frac{P_n(R_3,R_2)}{E_n(R_3,R_2)})f(k,n,i)\\&+\sum_{n=1}^{\infty}(c_n^{II}\frac{2R_2}{n\beta}\frac{2}{E_n(R_2,R_3)}+d_n^{II}\frac{2R_3}{n\beta}\frac{P_n(R_3,R_2)}{E_n(R_3,R_2)})g(k,n,i)\end{aligned} \tag{A.20}$$

$$b_k^i=\sum_{m=1}^{\infty}(a_m^j\frac{2\delta R_4}{m\pi\beta}\frac{P_{m\pi/\beta}(R_4,R_5)}{E_{m\pi/\beta}(R_4,R_5)}F(m,k) \tag{A.21}$$

$$\begin{aligned}&a_0^i+b_0^i\ln R_3=\\&\sum_{n=1}^{\infty}(a_n^{II}\frac{R_2}{n\beta}\frac{2}{E_n(R_2,R_3)}+b_n^{II}\frac{R_3}{n\beta}\frac{P_n(R_3,R_2)}{E_n(R_3,R_2)})r(n,i)\\&+\sum_{n=1}^{\infty}(c_n^{II}\frac{R_2}{n\beta}\frac{2}{E_n(R_2,R_3)}+d_n^{II}\frac{R_3}{n\beta}\frac{P_n(R_3,R_2)}{E_n(R_3,R_2)})s(n,i)\end{aligned} \tag{A.22}$$

$$\begin{aligned}&a_0^i+b_0^i\ln R_4=a_0^j+\frac{1}{2}\mu_0 J_j\left(R_5^2\ln R_4-\frac{R_4^2}{2}\right)+\\&\sum_{m=1}^{\infty}a_m^j\frac{2R_4}{\beta}\left(\frac{\delta}{m\pi}\right)^2\frac{P_{m\pi/\beta}(R_4,R_5)}{E_{m\pi/\beta}(R_4,R_5)}\sin\left(\frac{m\pi\beta}{2\delta}\right)\cos\left(\frac{m\pi}{2}\right)\end{aligned} \tag{A.23}$$

$$b_0^i=\frac{\delta}{\beta}\frac{1}{2}\mu_0 J_j\cdot\left(R_5^2-R_4^2\right)\quad\text{with}\quad i=j \tag{A.24}$$

where J_j is the current density in the slot *j*.

• Expression of the coefficient a_m^j for the *j*th slot subdomain

$$a_m^j = b_0^i \frac{4}{m\pi R_4} \sin\left(\frac{m\pi\beta}{2\delta}\right)\cos\left(\frac{m\pi}{2}\right) + \\ +\sum_{k=1}^{\infty}\left(a_k^i \frac{2}{E_{k\pi/\beta}(R_3,R_4)} - b_k^i \frac{P_{k\pi/\beta}(R_4,R_3)}{E_{k\pi/\beta}(R_3,R_4)}\right)\frac{2k\pi}{\delta\beta R_4} F(m,k) \tag{A.25}$$

We have to solve a system of linear equations whose dimension is equal to the number of unknowns. By rewriting the above equations in matrix and vectors format, a numerical solution can be found thanks to mathematical software (Matlab).

REFERENCES

[1] Z. Q. Zhu and D. Howe, "Instantaneous magnetic-field distribution in brushless permanent-magnet dc motor, part III: Effect of slotting," *IEEE Trans. Magn.*, vol. 29, no. 1, pp. 143-151, Jan. 1993.

[2] M. Markovic, M. Jufer, and Y. Perriard, "Reducing the cogging torque in brushless dc motors by using conformal mappings," *IEEE Trans. Magn.*, vol. 40, no. 2, pp. 451-455, Mar. 2004.

[3] K. Boughrara, D. Zarko, R. Ibtiouen, O. Touhami, and A. Rezzoug, "Magnetic field analysis of inset and surface-mounted permanent-magnet synchronous motor using Schwarz-Christoffel transformation," *IEEE Trans. Magn.*, vol. 45, no. 8, pp. 3166-3168, Aug. 2009.

[4] Q. Gu and H. Gao, "Effect of slotting in PM electrical machines," *Elect. Mach. Power Syst.*, vol. 10, pp. 273-284, 1985.

[5] N. Boules, "Prediction of no-load flux density distribution in permanent magnet machines," *IEEE Trans. Ind. Appl.*, vol. IA-21, no. 3, pp. 633-643, Jul./Aug. 1985.

[6] Z. Q. Zhu, and D. Howe, "Analytical prediction of the cogging torque in radial-field permanent magnet brushless motors," *IEEE Trans. Magn.*, vol. 28, no. 2, pp. 1371-1374, Mar. 1992.

[7] B. Ackermann and R. Sottek, "Analytical modeling of the cogging torque in permanent magnet motors," *Elect. Eng.*, vol. 78, no. 2, pp. 117-125, Mar. 1994.

[8] K. F. Rasmussen, H. D. John, T. J. E. Miller, M. I. McGilp, and O. Mircea, "Analytical and numerical computation of air-gap magnetic field in brushless motors with surface permanent magnet," *IEEE Trans. Magn.*, vol. 36, no. 6, pp. 1547-1554, Nov./ Dec. 2000.

[9] X. Wang, Q. Li, S. Wang, and Q. Li, "Analytical calculation of air-gap magnetic field distribution and instantaneous characteristics of brushless dc motors," *IEEE Trans. Energy. Convers.*, vol. 18, no. 3, pp. 424432, Sep. 2003.

[10] Z. J. liu, and J. T. Li, "Analytical solution of air-gap field in permanent magnet motors taking into account the effect of pole transition over slots," *IEEE Trans. Magn.*, vol. 43, no. 10, pp. 3872-3882, Oct. 2007.

[11] Z. J. liu, and J. T. Li, "Accurate prediction of magnetic field and magnetic forces in permanent magnet motor using an analytical solution," *IEEE Trans. Energy. Convers.*, vol. 23, no. 3, pp. 717-726, Sept. 2008.

[12] P. Kumar, and P. Bauer, "Improved analytical model of a permanent-magnet brushless DC motor," *IEEE Trans. Magn.*, vol. 44, no. 10, pp. 2299-2309, Oct. 2008.

[13] A. Bellara, Y. Amara, G. Barakat, and B. Dakyo, "Two-dimensional exact analytical solution of armature reaction field in slotted surface mounted PM radial flux synchronous machines," *IEEE Trans. Magn.*, vol. 45, no. 10, pp. 4534-4538, Oct. 2009.

[14] B. N. Cassimere, S. D. Sudhoff, and D. H. Sudhoff,"Analytical design model for surface mounted permanent-magnet synchronous machines," *IEEE Trans. Energy Convers.*, vol. 24, no. 2, pp. 347–357, June. 2009.

[15] F. Dubas, and C. Espanet "Analytical solution of the magnetic field in permanent-magnet motors taking into account slotting effect: no-load vector potential and flux density calculation," *IEEE Trans. Magn.*, vol. 45, no. 5, pp. 2097-21092, May 2009.

[16] T. Lubin, S. Mezani, and A. Rezzoug, "Exact analytical method for magnetic field computation in the air-gap of cylindrical electrical machines considering slotting effects," *IEEE Trans. Magn.*, vol. 46, no. 4, pp. 1092-1099, Apr. 2010.

[17] B. L. J. Gysen, K. J. Meessen, J. J. H. Paulides, and E. A. Lomonova, "General formulation of the electromagnetic field distribution in machines and devices using Fourier analysis," *IEEE Trans. Magn.*, vol. 46, no. 1, pp. 39-52, Jan. 2010.

[18] Z. Q. Zhu, L. J. Wu, and Z.P. Xia, "An accurate subdomain model for magnetic field computation in slotted surface-mounted permanent magnet machines," *IEEE Trans. Magn.*, vol. 46, no. 4, pp. 1100-1115, Apr. 2010.

[19] F. M. Sargos and A. Rezzoug, "Analytical calculation of airgap magnetic field produced by inset permanent magnet rotor machine," *J. Physics III* (in French), vol. 1, pp 103-110, 1990.

[20] Z. Q. Zhu, D. Howe, and Z. P. Xia,"Prediction of open-circuit airgap field distribution in brushless machines having an inset permanent magnet rotor topology," *IEEE Trans. Magn.*, vol. 30, no. 1, pp. 98-107, Jan. 1994.

[21] L. Jian, K. T. Chau, Y. Gong, C. Yu, and W. Li, "Analytical calculation of magnetic field in surface-inset permanent magnet motors," *IEEE Trans. Magn.*, vol. 45, no. 10, pp. 4688-4691, Oct. 2009.

[22] A. Rahideh, and T. Korakianitis, "Analytical magnetic field distribution of slotless brushless machines with inset permanent magnets," *IEEE Trans. Magn.*, vol. 47, no. 6, pp. 1763-1774, Jun. 2011.

[23] T. Lubin, S. Mezani, and A. Rezzoug, "2-D Exact analytical model for surface-mounted permanent-magnet motors with semi-closed slots," *IEEE Trans. Magn.*, vol. 47, no. 2, pp. 479-4929, Feb. 2011.

[24] D. C. Meeker, "Finite Element Method Magnetics", *Version 4.2 (1 April 2009 Build)*, http://www.femm.info

[25] S. J. Farlow, *Partial Differential Equations for Scientists and Engineers.* Dover publications, New York, 414 pp, 1993.

Thierry Lubin was born in Sedan, France, in 1970. He received the M.S. degree from the University of Paris 6, France in 1994 and the Ph.D. degree from the University Henri Poincaré, Nancy, France, in 2003.

He is currently a lecturer of Electrical Engineering at the University of Nancy at the Groupe de Recherche en Electrotechnique et Electronique de Nancy. His interests include modeling and control of electrical machines and applied superconductivity in electrical devices.

Smail Mezani was born in Algiers, Algeria, in 1974. He received the engineer diploma and the magister degree from the University of Sciences and Technology Houari Boumediene, Algiers, Algeria in 1996 and 1999 respectively. He obtained the Ph.D. degree from the Institut National Polytechnique de Lorraine, France, in 2004.

He is currently a lecturer at the University Henri Poincaré of Nancy, France, at the Groupe de Recherche en Electrotechnique et Electronique de Nancy where his research interests include the applications of superconductors in electromechanical devices.

Abderrezak Rezzoug received the electrical engineer degree from ENSEM INPL, Nancy, France in 1972, and the Dr. Ing. diploma and the Ph.D. degree from INPL, in 1979 and 1987 respectively.

After working at the INPL as an assistant Professor until 1991, he is currently a Professor of Electrical Engineering at the University Henri Poincaré, Nancy, France. As a member of the Groupe de Recherche en Electrotechnique et Electronique de Nancy, his main subjects of research concern superconducting applications to electrical devices, and the control and diagnosis of electrical machines.